Clays and Clay Minerals, Vol. 69, No. 4:463–476, 2021

ZIRCONIA-INTERCALATED KAOLINITE: SYNTHESIS, CHARACTERIZATION, AND EVALUATION OF METAL-ION REMOVAL ACTIVITY

Khaled S. Abou-El-Sherbini[1] *, Mohammed A. Wahba[1], Elsayed A. Drweesh[1], Adel I. M. Akarish[3], Seham A. Shaban[3], and Eman A. M. Elzahany[1]

[1]Department of Inorganic Chemistry, National Research Centre, 33 El Bohouth st. (former Eltahrir st.), Dokki, Giza 12622, Egypt
[2]Geological Sciences Department, National Research Centre, 33 El Bohouth st. (former Eltahrir st.), Dokki, Giza 12622, Egypt
[3]Department of Catalysis, Petroleum Refining Division, Egyptian Petroleum Research Institute, Cairo, Egypt

Abstract—The intercalation of kaolinite through the insertion of ions or molecules amongst the structural aluminosilicate layers is a vital process in numerous clay-based applications and products. Layer neutrality and hydrogen bonding limits direct intercalation into kaolinite, other than for small molecules. Synthesizing zirconia-intercalated kaolinite is not a straightforward matter. To overcome this barrier, raw Egyptian kaolin (UnK) or its acid-activated product (HK) was sonicated and impregnated in aqueous $ZrOCl_2 \cdot 8H_2O$ solution followed by thermal treatment at various temperatures (100, 200, 300, and 500°C). The intercalation process was confirmed using various spectroscopic and analytical techniques. The direct intercalation of ZrO_2 into the kaolinite layers was observed even through a mild thermal treatment (100, 200, and 300°C). The mechanism of intercalation was suggested to occur by binding ZrO_2 to the Si/AlO groups with a preference for the acid-activated HK, causing variable enlargements of the basal spacing and producing very perturbed layers. Interestingly, the surface area increased by 250% as a result of zirconia intercalation. Scanning electron microscopy (SEM) images showed a remarkable improvement in the stacking order of the kaolinite particles. The impact of ZrO_2 intercalation into kaolinite also enhanced its adsorption efficiency for Pb^{2+}, Cu^{2+}, and Cd^{2+} ions. Preliminary investigations showed that the zirconia-intercalated HK demonstrated a removal efficiency, which is three times greater than that of pristine HK. The adsorption tendency toward Pb^{2+} ions was greater than those of Cu^{2+} and Cd^{2+} and followed the order: $Pb^{2+} >> Cu^{2+} > Cd^{2+}$. The study suggests that the chemical modification of kaolin by zirconia via a direct intercalation technique, which greatly improves its functionality as demonstrated by the selective sorption of heavy metal ions, is worthy of further study.

Keywords—Sorption · Heavy metal ions · Intercalation · Kaolinite · Zirconia

INTRODUCTION

Kaolin is a clay consisting mainly of kaolinite but with minor quantities of quartz and feldspars. Kaolinite ($Al_2Si_2O_5(OH)_4$) has a 1:1 layered aluminosilicate structure, and the hydroxyl groups of the gibbsite sheets from one layer are attracted to the SiO_4 tetrahedral sheets of the next layer through hydrogen bonding (Bailey, 1966; Swindale, 1975) to form the kaolinite particles.

Kaolin is not particularly preferred as an adsorbent for hazardous cations (Jiang et al., 2013; Shirsath et al., 2013; Sari & Tuzen, 2014; Drweesh et al., 2016; Gao et al., 2016) because it has a small specific surface area (10–20 $m^2\ g^{-1}$) and a small ion-exchange capacity (15–75 μmol g^{-1}). Kaolin characteristics may be enhanced by functionalization with organic and inorganic substrates through various mechanisms such as chemical bonding, adsorption, and/or intercalation (Makó et al., 2016; Kristóf et al., 2018). The small electrostatic charge of the kaolinite layers and the hydrogen bonding between them makes the direct intercalation process more difficult than for other clay minerals, however (Ianchis et al., 2012; Zaharia et al., 2015). This hydrogen bonding may be broken by the intercalation of a few small polar guest molecules such as dimethyl sulfoxide (DMSO), urea, or salts such as potassium acetate (Ledoux & White, 1966; Olejnik et al., 1968; Tunney & Detellier, 1993; Dedzo & Detellier, 2016). Then, new hydrogen bonding develops; hence, this displacement method yields various intercalated compounds (Ianchis et al., 2012; Zaharia et al., 2015; Dedzo & Detellier, 2016; Ngnie et al., 2016).

The intercalation of kaolinite with inorganic salts through the reversible intercalation of kaolinite by CH_3COOK was pioneered by Wada (1961). Grinding of kaolinite with CH_3COOK resulted in a lattice expansion of the clay mineral and the appearance of a basal spacing of 14 Å caused by the expansion of the kaolinite lattice structure along the *c* axis (Wada, 1961). Another report (Singh & Mackinnon, 1999) declared the first successful intercalation of kaolinite by alkaline-earth halides. The kaolinite structure was first modified through a potassium acetate intercalation-deintercalation process, then subsequent intercalation by $CaCl_2$ and $MgCl_2$ was achieved and the kaolinite layers expanded to basal spacings of 9.8 and 10 Å, respectively (Singh & Mackinnon, 1999). A recent study reported the intercalation of the kaolinite structure by zinc ions and studied the shielding ability and the barrier efficiency of the unmodified and modified kaolinite on an epoxy ester coating (Majd et al., 2020). The Zn-intercalation yielded a small shift in the *d* spacing of the two most intense peaks of kaolinite from 7.10 and 3.56 Å to 7.11

* E-mail address of corresponding author: kh_sherbini@yahoo.com
DOI: 10.1007/s42860-021-00134-9

and 3.57 Å, respectively. Furthermore, Majd et al. (2020) reported a decrease in the intensities of XRD peaks in the Zn-kaolinite-intercalated powder and considered the decline in crystallinity as proof of successful Zn intercalation. The incorporation of inorganic cations, in particular, into clay minerals often enhances the suitability of the clay as a sorbent, catalyst support, or ion exchanger. These characteristics derive from the development of larger interlayer spaces, a three-dimensional porous structure, new acidic sites, and/or larger surface area while maintaining better thermal stability (Mnasri & Frini-Srasra, 2013; Ngnie et al., 2016). Beside the inherent acidity of the clay layers, the guest itself may also possess an acidic character.

Very few studies have reported the incorporation of Zr into kaolinite, though Vaughan (1994) patented hydrothermal synthesis of zirconium oxide-pillared interlayered kandites using zirconium oxychloride ($ZrOCl_2$) in acetic acid at 100°C, resulting in a *d* value of the basal spacing ≥14.5 Å. The main limitation of this method is the use of a closed system for the hydrothermal treatment, which limits large-scale production. Synthesis of poly(oxozirconium)-kaolinite by stirring a 0.1 M solution of $ZrOCl_2$ with kaolin was also reported but with no evidence of accompanying enlargement of the basal spacing. The adsorption of Cu^{2+} (Bhattacharyya & Gupta, 2006), Cd^{2+} (Gupta & Bhattacharyya, 2006), Pb^{2+} (Gupta & Bhattacharyya, 2005), Fe^{3+}, Co^{2+}, and Ni^{2+}(Bhattacharyya & Gupta, 2008) from aqueous solution was evaluated. The adsorption capacity of the modified kaolinite was not improved in comparison with the pristine sample. From a commercial point of view, nanocrystalline zirconia itself is an important material and used extensively as an anodic material in solid oxide fuel cells, as a catalyst in oxygen-sensor applications, and as a structural material (Miura et al., 2014; Agarkov et al., 2018; Wang et al., 2019).

Efficient incorporation of Zr into kaolinite without limitation is still a challenge, especially for large-scale production. The objectives of the current study were to find a simple, scalable synthesis method of zirconia-intercalated kaolinite, and to test the possible applications of the modified kaolinite as a selective sorbent for Cd^{2+}, Cu^{2+}, or Pb^{2+} from water.

EXPERIMENTAL

Material

The characterization of the untreated raw Egyptian kaolin sample collected from the Wadi El Hamadiya area, south Sinai, Egypt, was reported previously (Drweesh et al., 2016). The major elements are SiO_2 (47.97%), Al_2O_3 (34.74%), TiO_2 (2.26%), and Fe_2O_3 (1.46%). The kaolin loss on ignition (LOI) is 12.55%. Firstly, raw kaolin was ball-milled, sieved to <112 μm, and labeled as UnK. UnK was activated with 5.0 mol L^{-1} HCl as reported previously (Drweesh et al., 2016) and labeled as "HCl-treated kaolin" (abbreviated HK). Kaolinite was the main constituent in both UnK and HK with concentrations of 89.9 and 83.8%, respectively, and exhibiting a Hinckley index of 0.58 indicating that it is a highly disordered kaolinite (Abou-El-Sherbini et al., 2017). $ZrOCl_2{\cdot}8H_2O$ (99.0%) was purchased from Merck (Darmstadt, Germany - B372317 439). Experimental solutions containing heavy-metal ions were prepared by dissolving stoichiometric amounts of $Pb(NO_3)_2$, $Cu(NO_3)_2$, and $Cd(NO_3)_2$(from Sigma-Aldrich, Steinheim, Germany) in deionized water at the desired concentrations. The pH of solutions was adjusted using 0.1 M NaOH (Merck, Darmstadt, Germany) and/or 0.1 M HNO_3 (El-Nasr Co., Cairo, Egypt).

Equipment

The kaolin samples were subjected to powder X-ray diffraction (XRD) analysis to determine their mineralogical compositions using CuKα radiation and a Ni filter at a constant voltage of 40 kV and current of 30 mA, using an Empyrean Powder Diffractometer (Malvern Panalytical Ltd, Malvern, UK) with a side-loading sample holder to minimize mineral orientation. Chemical analyses for the major oxides (mass%) and some minor elements of the raw kaolin and the modified samples were performed using X-ray fluorescence spectrometry (XRF) on a wavelength-dispersive spectrometer (Axios, WD-XRF Spectrometer, PANalytical, 2005, Lelyweg, The Netherlands). Thermogravimetric analysis (TGA) was performed using an SDT Q600 thermal analyzer (TA Instruments, New Castle, Delaware, USA) at a heating rate of 10°C min^{-1} under N_2. TGA was also performed with a Perkin Elmer 7-Series thermal analyzer (Waltham, Massachusetts, USA) at a heating rate of 10°C min^{-1} in air. Fourier-transform infrared (FTIR) spectra were recorded on a Nicolet iS10 (Thermo-Fisher Scientific, Waltham, Massachusetts, USA) using a KBr pellet at ~0.5% sample concentration. Scanning electron microscopy (SEM) images of the gold-coated samples were performed using SEM model Quanta FEG 250 (FEI, Hillsboro, Oregon, USA) equipped with an energy dispersive X-ray analysis (EDX) unit, with accelerating voltage of 30 kV (FEI Company, Eindhoven, Noord-Brabant, The Netherlands). Elemental mapping analysis was performed using a field emission scanning electron microscope model Zeiss Sigma 300 vp (Oberkochen, Germany). Transmission electron microscopy (TEM) measurements were performed on a JEOL model 1200EX electron microscope (Peabody, Massachusetts, USA) operated at an accelerating voltage of 120 kV. Selected area electron diffraction (TEM-SAED) was recorded using the TEM. The sample was prepared by dropwise coating of its acetone suspension on carbon-coated copper TEM grids (40 μm×40 μm mesh size). The sample was dried under vacuum in a desiccator before loading into a specimen holder. Size-distribution analysis was performed on aqueous sample suspensions by using a Zeta Sizer, ZS-Nano instrument, from Malvern Instruments (Malvern, UK). Surface area (S_{BET}) was determined with a Nova surface area analyzer 3200 (Quantachrome, Boynton Beach, Florida, USA) using nitrogen at 77 K. The S_{BET} was determined following the BET method (Brunauer et al., 1938). 0.06–0.1 g of prepared sample was outgassed at 300°C for 24 h in order to remove the water adsorbed in the sample and liquid nitrogen was used during the nitrogen adsorption-desorption analysis at –196°C. Pore-size distribution (PSD) curves were calculated from the

https://doi.org/10.1007/s42860-021-00134-9 Published online by Cambridge University Press

adsorption branch of the isotherms using the Barrett-Joyner-Halenda(BJH) method (Barrett et al., 1951). The residual concentration of Cd^{2+}, Cu^{2+}, or Pb^{2+} was determined using the APHA3111 standard method (Baird et al., 2017) on a Varian 220 flame atomic absorption spectrophotometer (FAAS) (Varian, Inc. Palo Alto, California, USA). For each series of measurements, the absorption calibration curve was constructed from a blank and three standards.

The pH of the solution of each sample was adjusted with NaOH and HNO_3 solutions using a Hanna Instruments 8519 pH/mV meter (Padova, Italy), with an expanded scale and an accuracy of ±0.1.

Methodology

Intercalation of Zr(IV) into the acid-activated (HK) and untreated (UnK) kaolin. UnK or HK (10 g) was added to 10 mL of distilled H_2O, impregnated for a week in a stoppered 250 mL glass conical flask to guarantee sufficient hydration of kaolinite layers, then $ZrOCl_2{\cdot}8H_2O$ (19.69 g ≡ 0.061) was added and mixed thoroughly. Using a high concentration of $ZrOCl_2$ (6.1 mol L^{-1}) was important to avoid hydrolysis (Solovkin & Tsvetkova, 1962). The slurry was sonicated for 60 min and impregnated again for 6 days with frequent shaking. For analysis purposes, 1 g was separated after this stage, dried at 70°C, and labeled as HKZS. The mixture was dried gradually at 100°C for 24 h (labeled as UnKZS100 and HKZS100, respectively), then heated again at 200°C for 60 min, washed with 10 mL of 0.1 mol L^{-1} HCl and then with 50 mL of distilled water, dried at 105°C, and labeled as UnKZS200 and HKZS200, respectively. Finally, the UnKZS200 or HKZS200 was heated at 300 and 500°C for 3 h and labeled as UnKZS300 and UnKZS500 or HKZS300 and HKZS500, respectively. For the sake of comparison, the same procedure for the synthesis of HKZS200 was repeated without HK to evaluate the effect of wet aging, sonication, and thermal treatment on $ZrOCl_2{\cdot}8H_2O$. The samples produced were labeled as $ZrOCl_2$-S, $ZrOCl_2$-S100, and $ZrOCl_2$-S200 for the samples heated at 70, 100, and 200°C, respectively. In addition, the synthesis of HKZS-100 was repeated, replacing $ZrOCl_2{\cdot}8H_2O$ and water with 10 mL of concentrated HCl (36–37%) to resemble the acidity produced during the hydrolysis of $ZrOCl_2{\cdot}8H_2O$. The samples produced were labeled as HK-S-HCl, HK-S-HCl100, and HK-S-HCl200 and were heated at 70, 100, and 200°C, respectively. HK was also heated at 300 and 500°C, and similarly labeled as HK300 and HK500, respectively. Detailed names, labels, and synthesis parameters are given in the Supplementary Material (Table S1).

Adsorption of Cd^{2+}, Cu^{2+}, or Pb^{2+}. The adsorption experiments were carried out at room temperature (~25°C). To investigate the effect of the initial pH on the adsorption behavior of Cd^{2+}, Cu^{2+}, or Pb^{2+}, a 10 mL volume (v) with an initial concentration of 10 mg L^{-1} (C_i) of the metal ions (as nitrate) was added to a mass (m) of 10 mg of HK or HKZS300. The resulting solutions containing adsorbent were agitated for 60 min. The initial pH values, 1.87, 3.0, 5.0 (acetate-buffered), and 8.0 (ammonia-buffered), were controlled using 0.1 M NaOH and HNO_3 solutions. The suspensions were filtered and the final concentration of metal ions in solution (C_f) was determined by FAAS. The removal efficiencies (E, %) of the metal ions onto HK or HKZS300 were calculated using the following equation:

$$E = \frac{(C_i - C_f)}{C_i} 100(\%) \quad (1)$$

The distribution coefficient of the metal ions ($K_{d,\ M}$) and the selectivity coefficient ($S_{M1/M2}$) were calculated using the following equations:

$$K_{d,M} = \frac{(C_i - C_f) \cdot v}{C_f \cdot\ m} \left(mLg^{-1}\right) \quad (2)$$

$$S_{M1/M2} = \frac{K_{d,\ M1}}{K_{d,M2}} \quad (3)$$

RESULTS AND DISCUSSION

Characterization

XRD/TG studies. X-ray diffraction (Fig. 1) traces indicated the effect of zirconium oxychloride on kaolinite in the raw inactivated kaolin (UnK) and the HCl-activated kaolin (HK) after homogenizing mixtures by a sonication-impregnation technique and heating the products at 100, 200, 300, or 500°C. The XRD pattern of the parent materials (UnK and HK) were typical of kaolin and similar to those obtained previously with d_{001} values for kaolinite of 7.19 Å (Drweesh et al., 2016). The XRD pattern of $ZrOCl_2{\cdot}8H_2O$ was also typical of a pure substance (ICSD 00-032-1498).

Within the present XRD parameters, no decisive evidence of the intercalation of ZrO_2 into kaolinite layers of the $ZrOCl_2$-treated kaolins could be observed. A remarkable decrease in the intensity of the kaolinite reflections was observed, however, especially that of the basal spacing (d_{001}) of kaolinite phases compared with the d_{101} reflection of quartz at 3.34 Å in the parent kaolins (UnK and HK) and concentrated HCl-treated HK blanks (HK-S-HCl100 and HK-S-HCl200). Although new, broad reflections were observed, with greater d_{001} values of 10.7–13.6 Å, for the $ZrOCl_2$-treated samples dried at 100–200°C, which are close to the reported basal spacing of meta-kandite intercalated with ZrO_2– 14.5 Å (Vaughan, 1994), they may also be due to the residues of incompletely decomposed $ZrOCl_2{\cdot}8H_2O$ when compared with the diffraction patterns of $ZrOCl_2$-S100 and $ZrOCl_2$-S200. Relative broadening as well as the decrease in intensity of basal spacing peaks, compared to the parent clay mineral, were reported to be good evidence for the existence of successful intercalation, and/or an irregular-packing of intercalated and non-intercalated layers (Valverde et al., 2003; Majd et al., 2020). In addition, the intercalation of kaolinite, in particular, may reduce XRD quality due to the generation of lattice

https://doi.org/10.1007/s42860-021-00134-9 Published online by Cambridge University Press

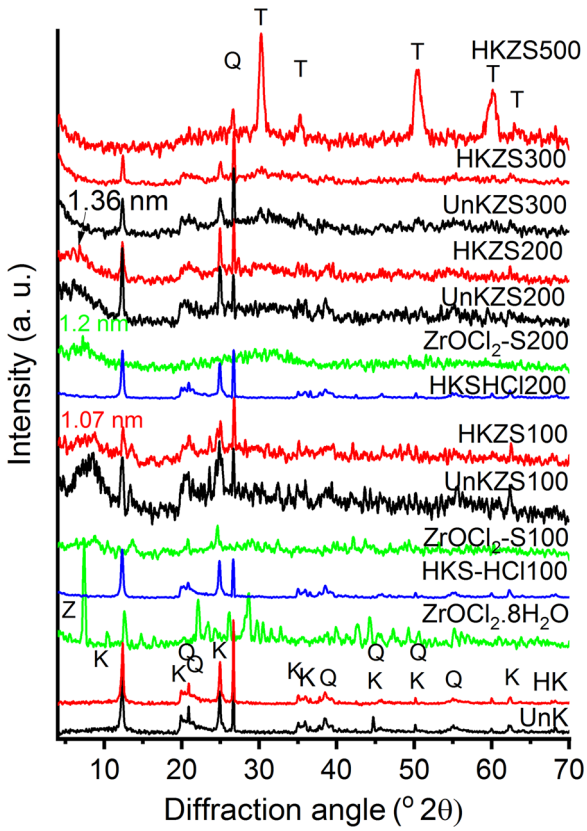

Fig. 1. XRD patterns of UnK, HK, $ZrOCl_2{\cdot}8H_2O$, and their ZrO_2-modified products. K, Q, Z, and T denote kaolinite, quartz, $ZrOCl_2{\cdot}8H_2O$, and tetragonal zirconia, respectively

perturbation, defects, and disorders in the structure (Grzybek et al., 2001).

Zr(IV)-intercalation in other clays was reported (Ohtsuka et al., 1993; Chaabene et al., 2004; Valášková et al., 2013). Two models of Zr-tetrameric cations ($[Zr_4(OH)_{14}(H_2O)_{10}]^{2+}$ and $[Zr_4(OH)_8(H_2O)_{16}]^{8+}$, and one model of Zr-octameric cation ($[Zr_8(OH)_{20}(H_2O)_{24}]^{12+}$) were built; only the tetrameric models were studied for intercalation into vermiculite because the octameric cation was excluded due to its thickness (1.0 nm) being greater than that of the vermiculite layer (0.86 nm) (Valášková et al., 2013). The insertion of Zr-tetrameric cations into vermiculite was suggested to yield a d_{002} of 14.2 Å. Successful Zr(IV)-intercalation in montmorillonite was also reported to have a van der Waals' spacing of 11.4 or 7.0 Å (Ohtsuka et al., 1993; Chaabene et al., 2004), assigned to hosting of octamer $[Zr_8(OH)_{20}(H_2O)_{24}Cl_{12}]^{4+}$ or tetramer $[Zr_4(OH)_8(H_2O)_{16}Cl_6]^{2+}$, respectively.

According to the length and thickness of the $[Zr_4(OH)_{12}(H_2O)_{12}]^{4+}$ polycation estimated to be 9.1 and 5.5 Å, respectively (Miehé-Brendlé et al., 1997), the intercalation form of Zr(IV) in the Zr-modified kaolin samples is supposed to proceed in two steps: (1) $ZrOCl_2{\cdot}8H_2O$ undergoes hydrolysis which increases with temperature (Matsui & Ohgai, 2002), to form tetramers $[Zr_4(OH)_8(H_2O)_{16}]^{8+}$ or more complex polyoxide polymers. (2) The resultant hydrated tetramers are bonded to the kaolinite layers with face-to-face or edge-to-edge positioning parallel to the *xy* plane as the unit kaolinite layer thickness is ~5.4 Å (Zhang et al., 2017).

Comparing the diffraction patterns of UnKZS100-300 ($ZrOCl_2$-treated inactivated kaolin) with HCl-activated analogs HKZS100–300, the ratio of intensities of the 00*l* lines of kaolinite to the quartz reflection at 3.34 Å, accounting for the d_{101} of quartz, were observed to decrease in the HK-activated kaolin compared with untreated kaolin, which may indicate that the ZrO_2 binding process is enhanced by the acid-activation of the kaolinite surface. This may be attributed to the release of more surface OH groups upon acid activation (Drweesh et al., 2016).

The ~13 Å *d* value was not observed by XRD for the samples heated at 300 or 500°C (Fig. 1), while sustaining a remarkable reduction in the parent d_{001} intensity relative to the *d* value at 3.34 Å accounting for the d_{101} reflection of quartz. The increase of background intensity at >8°2θ for both UnKZS300 and HKZS300 may be due to the polymerization of intercalated zirconia building units with increasing temperature yielding an amorphous kaolinite with an enlarged perturbed structure. Polymerization of the intercalated Zr(IV) species was suggested to form zirconia sandwiched face-to-face or edge-to-edge between less ordered stacking of the kaolinite layers. The polymerization of tetramer and octamer forms of Zr(IV) was reported to be enhanced with calcination yielding crystalline zirconia (Farfan-Torres et al., 1992; Chaabene et al., 2004).

A loss of the uniform layered packing in the *xy* plane of Zr-modified kaolinite layers may accompany thermal treatment that causes aggregation of zirconia particles and weakens bonding between kaolinite layers with ZrO_2. This explanation is supported by XRD (Fig. 1) via the disappearance of kaolinite reflections (due to the dehydration of the kaolinite and the formation of metakaolinite (Gil et al., 2001)) and the development of a ZrO_2 metastable tetragonal phase [PDF80-0965] at 500°C. Obtaining the tetragonal ZrO_2 metastable phase at such a low temperature is interesting due to its catalytic importance (Vera et al., 2002), knowing that it crystallizes at a temperature of 1205°C (Chevalier et al., 2009), or at lower temperature by using special calcination conditions such as the presence of silica or alumina as supporting materials (Nagarajan & Rao, 1990).

TGA. In order to understand the mechanism further, a TGA measurement (Fig 2) was performed for the $ZrOCl_2{\cdot}8H_2O$ and HKZS sample that was dried at 70°C without further thermal treatment. The TGA of $ZrOCl_2{\cdot}8H_2O$ showed the presence of five mass-loss stages, with T_{max} at 113, 162, 286, 343, and 460°C, which corresponded to mass-loss stages of 25.3, 18.3, 10.2, 3.1, and 3.4%, respectively. These results are close to the thermal decomposition of $ZrOCl_2{\cdot}8H_2O$, performed in air, reported to occur in two major mass-loss stages (Takagi, 1954; Gorodylova et al., 2014; Gorodylova & Šulcová, 2018), which help to explain the $ZrOCl_2{\cdot}8H_2O$/HK reaction. A release of crystalline water was reported within the range 70–230°C, leading to the formation of XRD-amorphous $ZrOCl_2$ as

https://doi.org/10.1007/s42860-021-00134-9 Published online by Cambridge University Press

illustrated in Eq. 4. In the temperature range of 230–500°C, $ZrOCl_2$ reacts with atmospheric water to form amorphous ZrO_2 and HCl is released as shown by Eq. 5. A small exothermic effect was observed with a maximum rate at 500°C that can be associated with the crystallization of monoclinic ZrO_2(Beden & Guillaum, 1969) as represented by Eq. 6.

$$ZrOCl_2 \cdot 8H_2O \overset{70-230^{\circ}C}{\rightarrow} ZrOCl_2 + 8H_2O \quad (4)$$

$$ZrOCl_2 + H_2O \overset{230-500^{\circ}C}{\rightarrow} amorphous ZrO_2 + 2HCl \quad (5)$$

$$amorphous ZrO_2 \overset{500^{\circ}C}{\rightarrow} monoclinic ZrO_2 \quad (6)$$

The TGA of the HKZS (Fig. 2) showed the presence of four principal mass-loss stages at T_{max} 48.9, 130.8, 261.0, and 436.6–472.6°C, which correspond to 2.90, 11.92, 9.15, and 9.37% of mass-loss stages, respectively.

On the other hand, TGA of HK was reported to show two main mass-loss stages at 25–75°C and 490°C, which were attributed to elimination of the adsorbed H_2O and dehydroxylation of kaolinite aluminols, respectively (Drweesh et al., 2016), as explained in Eq. 7.

$$Al_2Si_2O_5(OH)_4 \rightarrow Al_2Si_2O_7 + 2H_2O \quad (7)$$

Accordingly, the first and second stages in the present TGA study of HKZS (Fig. 2) were attributed to the loss of water (either adsorbed on kaolin or crystallized in $ZrOCl_2 \cdot 8H_2O$) and HCl. The formation of white clouds in the ammonia solution test indicated the evolution of HCl gas, beginning from 70°C. The third stage may have been related to the loss of most chloride content, as revealed from the EDX measurement of the HKZS300 (Fig. S2) and the elemental mapping results (Fig. S3), which differed from the reported thermal decomposition of $ZrOCl_2 \cdot 8H_2O$ to amorphous ZrO_2(Eq. 6), that may be physically or chemically bonded to perturbed kaolinite layers as suggested by the XRD study.

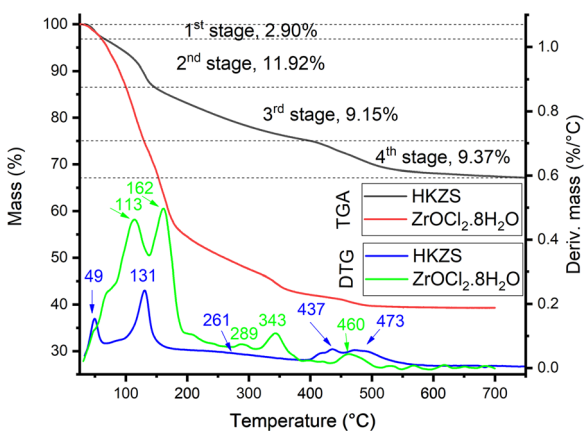

Fig. 2. TGA and DTG of $ZrOCl_2 \cdot 8H_2O$ and impregnated $ZrOCl_2 \cdot 8H_2O$ + HK (HKZS) at a heating rate of 10°C/min under N_2

The last TGA stage, which showed a remarkable reduction in the offset-temperature of the stage of HK (490°C) (Drweesh et al., 2016), was composed of multiple overlapped thermal decomposition reactions. During this stage, dehydroxylation of aluminol groups clearly took place. Accordingly, the existence of the dehydroxylation stage below 500°C and its complex structure are evidence of the bonding of the kaolinite layers with the intercalated ZrO_2(Kristó et al., 1997; Cheng et al., 2012).

The last stage was accompanied by the crystallization of the tetragonal ZrO_2 as concluded from the XRD pattern of the HKZS500 (Fig. 1), contrary to the expected monoclinic form reported in the literature for the thermal treatment of $ZrOCl_2.8H_2O$ in air (Gorodylova et al., 2014). This may be attributed to the influence of kaolinite as a support for the crystallization process of ZrO_2.

XRF. Analysis by XRF of UnK and HK and their zirconia-modified kaolins UnKZS300 and HKZS300 (Table 1) gave results which were very similar to those from EDX measurements (Fig. S3), indicating the homogeneity of the sample despite the presence of separate phases of silica-, titania-, and zirconia-rich kaolinite. The XRF indicated that Si/Al atomic ratios increased to 1.383 and 1.631 in UnKZS300 and HKZS300 compared with their initial values (1.226 and 1.258) in the parent samples UnK and HK, respectively. On the other hand, Cl/Zr atomic ratios decreased from the theoretical 2:1 in $ZrOCl_2 \cdot 8H_2O$ to only 0.329 and 0.272 for UnKZS300 and HKZS300, respectively. These results suggest a partial release of Al as $AlCl_3$ from the kaolinite lattice as a result of the thermal treatment of zirconyl chloride with kaolin

Table 1. XRF analysis of UnK and HK and their zirconia-modified kaolins

Oxide	Mass (%)			
	UnK	HK	UnKZS300	HKZS300
SiO_2	49.34	50.17	32.674	35.552
Al_2O_3	34.15	33.85	20.044	18.491
TiO_2	1.84	2.16	1.009	0.912
Fe_2O_3	1.42	1.31	0.705	0.706
ZrO_2	0.104	0.105	30.921	30.860
MgO	0.11	0.06	0.054	0.056
CaO	0.12	0.03	0.058	0.024
Na_2O	0.10	0.02	0.171	0.059
K_2O	0.06	0.08	0.028	0.025
CuO	0.01	0.003	0.023	0.012
ZnO	0.008	0.010	0.007	0.010
P_2O_5	0.07	0.07	0.087	0.095
Cl^-	0.03	0.21	2.932	2.420
LOI	12.45	11.70	11.10	10.35

As determined by loss on ignition (LOI), the kaolinite percentages were 89.28 and 83.90% in UnK and HK, respectively

https://doi.org/10.1007/s42860-021-00134-9 Published online by Cambridge University Press

at temperatures up to 300°C according to Eq. 8.

$$5/2\ x\mathrm{ZrOCl_2} + \mathrm{Al_2Si_2O_5(OH)_4} \xrightarrow{300°C} \text{amorphous} \quad (8)$$

$$\mathrm{ZrO_2/Al_{2-x}Si_2O_5(OH)_{4-2x}} + x\mathrm{AlCl_3} + 2x\mathrm{HCl}$$

The atomic ratios of Zr/Al in UnKZS300 and HKZS300 (0.637 and 0.691) were also smaller than the starting values of UnK and HK (0.912 and 0.920). These results mean that the loading efficiency of zirconia with respect to kaolinite in HKZS300 is greater than that of UnKZS300 where zirconia loading efficiencies were 69.8 and 75.1%, respectively.

On the other hand, metal contents in the acid-activated samples were slightly less than those for the untreated samples, indicating the leaching effect of HCl that releases the OH groups engaged in bonding with the leached metal ions; this was also reported previously (Drweesh et al., 2016).

FTIR. The FTIR spectra (Fig. 3) obtained for the $ZrOCl_2{\cdot}8H_2O$, UnK, HK, HK-S-HCl, HK300, and HK500 samples and their kaolin-ZrO_2-modified products showed, for UnK, HK, and HK-S-HCl, three strong absorption bands centered at 3697, 3654, and 3622 cm^{-1}, corresponding to the inter- and intra-hydroxyl groups (Farmer & Russell, 1964; Frost et al., 1998; Abou-El-Sherbini et al., 2017). The bands at ~1626 and ~3430 cm^{-1} correspond to the bending and stretching modes of the OH groups of water molecules. The bands centered at 1111, 1034, 1005, 938, 913, 792,753, 694, 537, 469, and 428 cm^{-1} are assignable to the apical Si–O stretching, two in-plane Si–O–Si stretching, inner Al–OH bending, inner surface Al–OH bending, three OH translational, Si–O–Al in-plane bending deformation, Si–O bending, and Si–O vibrations, respectively, which are typically the IR absorption bands of kaolinite (Frost & Vassallo, 1996). The FTIR spectra of HK300 showed a 1–2 cm^{-1} blue shift in the wavenumber positions of stretching modes of the inner and inner surface hydroxyl-group vibrations while in HK500 all Al–O–H-including vibration bands disappeared due to the dehydroxylation of aluminols and the formation of the amorphous metakaolinite phase (Frost & Vassallo, 1996). Also, new broad bands appeared at 1080 and 799 cm^{-1}, ascribed to the Si–O and AlO_4 vibrations, respectively, in the newly formed metakaolinite (Ilić et al., 2010). The FTIR spectra of both $ZrOCl_2.8H_2O$ and $ZrOCl_2$-S showed strong absorption bands at 3000–3500 cm^{-1}(broad) and 1620–1624 cm^{-1} due to ν_{OH} and δ_{OH} vibrations of water molecules. Much weaker absorption bands at 545–548, 438–439, and 407–415 cm^{-1} are due to Zr–O (Štefanić et al., 1996).

By comparing the FTIR spectra of HK and HK300 with those of HKZS, HKZS300, and UnKZS300, the effect of the Zr(IV) coating on the kaolinite structure was confirmed by the observed 2 cm^{-1} red shift in the stretching modes of the inner and inner-surface hydroxyl-group vibrations (especially in HKZS300), the remarkable weakness of the surface stretching AlO–H vibrations, and a red-shift of 15 cm^{-1} of the stretching mode of the OH groups of water molecules at 3430 cm^{-1}. Also, the bands due to Zr–O at 407–415 and 438–439 cm^{-1} in $ZrOCl_2{\cdot}8H_2O$ and $ZrOCl_2$-S were blue-shifted to 420 and 449 cm^{-1} in the FTIR spectra of HKZS but could not be distinguished in the other zirconia-modified kaolin samples. The interaction of OH, Si–O, and aluminol groups with the Zr(IV) species confirmed the intercalation of zirconia and the presence of strong bonding with kaolinite surface as concluded elsewhere with another aluminosilicate support; SBA-15(Gong et al., 2011).

In addition, the FTIR spectra of UnKZS500 and HKZS500 support the intercalation process of zirconia through the remarkable decrease of bands due to AlO_4 vibrations in the metakaolinite, in addition to the appearance of multiple weak bands in the region of the inner and inner-surface OH-group vibrations for HKZS500, which confirmed the strong interaction between aluminols and zirconia. The blue shift of hydroxyl-stretching vibrations was reported to indicate weaker hydrogen bonding, corresponding to the structural OH groups with the higher energies (i.e. wavenumbers) and the weaker

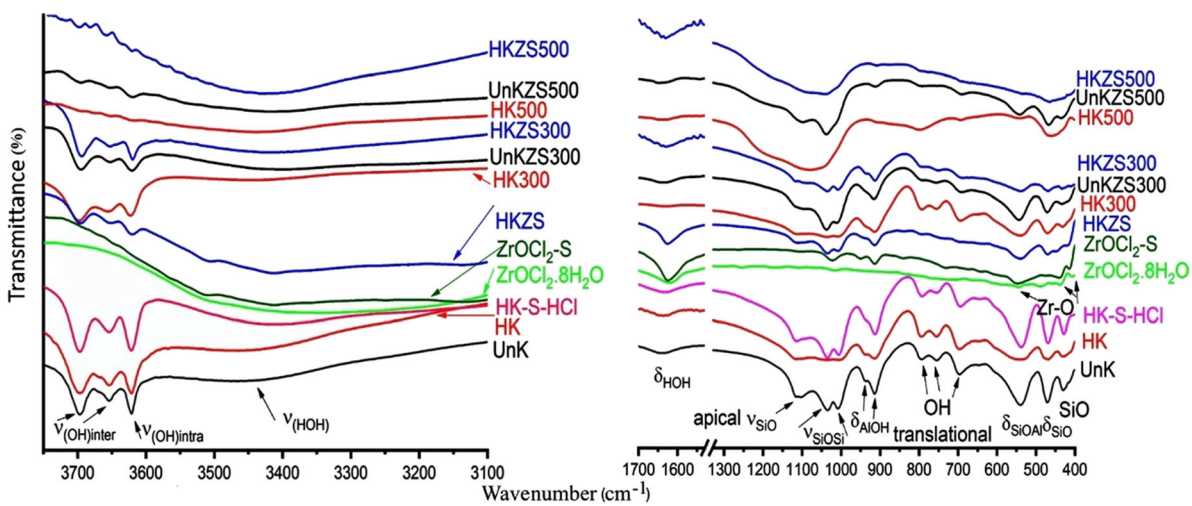

Fig. 3. FTIR spectra of HK, HK300, HK500, and their ZrO_2-modified products

https://doi.org/10.1007/s42860-021-00134-9 Published online by Cambridge University Press

Table 2. Locations and assignment of FTIR absorption bands (cm^{-1}) of kaolin and its zirconia-modified samples

Sample	UnK	HK	HK-HCl-S	HKZS	HK300	UnKZS300	HKZS300	HK500	UnKZS500	HKZS500	$ZrOCl_2$ $8H_2O$	$ZrOCl_2$-S
$\nu_{(OH)inter}$	3697	3697	3697	3696	3698	3695	3694	----	3696 (vw)	3697 (vw)		
	3668	3669	------	------	----	-------	3665	-----	3681 (vw)	3681 (vw)		
	3653	3654	3653	3652	3655	3652	3652	-----	3652 (vw)	3658 (vw)		
$\nu_{(OH)intra}$	3621	3621	3622	3620	3622	3620	3620	3622	3619 (w)	3621 (w)		
$\nu_{(HOH)}$	3450	3450	3415	3412	3430	3420	3413	3435	3417 (w)	3423 (w)	3340	3412
$\delta_{(HOH)}$	1634	1628	1634	1625	1629	1629	1630	1630	1636	1633	1621	1624
ν_{Si-O}	1113	1114	1114	1111	1111	1111	1113	1095	1099	1089		
ν_{SiOSi}	1033	1035	1035	1036	1035	1038	1035	1078	1037	1049		
	1006	1007	1006	1008	1007	1010	1007		1010			
$\delta_{(Al–OH)}$	938	938	936	940	937	940	935	----	---	----		
inner and inner-surface	913	914	913	914	914	916	914	910	910	910		
ZrOH												913
OH translational	792	790	790	790	790	793	793	790	791	791		
	754	754	755	754	753	754	750	---	----	-----		
	694	694	693	693	693	694	695	693	689	689		
Si-O-Al in plane bending (def)	537	537	538	539	539	538	538	541	542	-----		
Si-O bending	470	470	469	470	470	469	469	470	468	465		
Si-O vibrations	430	430	429	425	431	431	433	431	431	431		
Zr-O											723	731
											545	672
											489	639
											457	548
											438	474
											407	440
												415

vw: very weak, w: weak, def: deformation

participation in the hydrogen bonding (Libowitzky & Beran, 2004). Accordingly, the observed red shift accompanying zirconia upload may be correlated with O–H stretching frequencies and O–H…..O stronger hydrogen bond strength due to the coating with zirconia (Libowitzky, 1999). A summary (Table 2) was given for the FTIR absorption spectra (cm^{-1}) of kaolin and its zirconia-modified samples.

SEM. Examination of HK by SEM (Fig. 4a) indicated that kaolinite is found as discrete, coarse aggregates, poorly crystallized with irregular geometry that might reflect its detrital nature. In addition, silt-sized quartz grains were present. The SEM image of HKZS300 (Fig. 4b) revealed improvement in the lamellar crystalline nature of the clay, as well as a uniform distribution of Zr over all of the face-to-face- and edge-to-edge-ordered clay layers as confirmed by the EDX measurement (Fig. S3), despite the presence of minor constituents of ZrO_2-rich/kaolinite. Zeta size mapping (Fig. S4) confirmed these large differences in the morphologies of HK and HKZS300. Although HK was polydispersed, mainly due to the presence of sedimentary particles, it showed a high population of particles having a diameter of 1 μm, while the HKZS300 sample was not suitable for DLS measurements due to its polydispersed nature. The HKZS300 contained large particles and aggregates with an average size larger than the upper size display limit of the Zeta Sizer instrument (10 μm). The presence of zirconia in the HKZS300 led to binding of the layers with kaolinite particles.

TEM. Transmission electron microscopy images for HKZS300 (Fig. 5a–h) support the presence of zirconia-intercalated kaolinite phases with basal spacings of ~11 to 25 Å, as illustrated in Fig. 5h, while the 7.16 Å d_{001} value of the parent kaolinite is present also. Both kaolinite phases, the pristine and the enlarged, could be recognized easily even in the same particle (regions A and B in Fig. 5c). The modified kaolinite crystallites were observed to be darker on their edges than in their centers (Fig. 5d, f). A TEM-SAED pattern of kaolinite layers (Fig. 5d, e) also showed well-defined spots with *d* spacings of ~21.49 Å. These observations may be explained by assuming gradient contents of intercalated zirconia into kaolinite interlayer space that decrease toward the kaolinite crystallite center. The observed darker edges compared to centers of particles (Fig. 5d, f) support the suggested cement-like action of zirconia to the kaolinite particles, which in turn led to enhancement of the stacking order of the kaolinite particles. In addition, the kaolinite layers appeared thicker by variable levels than their ideal 5.4 Å thickness of the silica-gibbsite layer (Fig. 5g, h). The outer surface of the kaolinite crystallites in the XY plane was observed to be coated with a layer of nano-sized dark particles of 1.8 nm diameter, capturing nanopores within them (Fig. 5g); these may be zirconia nano-particles formed by dimerization or higher polymerization of zirconia tetramers. The enlarged kaolinite phase was observed to be wavy and strongly perturbed, which explains the poor-quality XRD patterns of zirconia-modified kaolin samples. Partial intercalation of $ZrOCl_2 \cdot 8H_2O$ into kaolinite occurred at temperatures of up to 500°C (Fig. 6).

Texture study. The N_2adsorption/desorption isotherms and pore-size distributions (Fig. 7a, b**,** respectively) were performed for HK and its zirconia-modified product, HKZS300. Three well distinguished regions of the adsorption isotherm were evident: (1)monolayer-multilayer adsorption; (2) capillary condensation; and (3) multilayer adsorption on the outer surfaces of the particles. HK samples have the type II isotherm with a distinct capillary condensation step, which is characteristic of mesoporous materials according to the classification of the International Union of Pure and Applied Chemistry (IUPAC). Nitrogen adsorption-desorption isotherms of HK illustrated a clear H4 type hysteresis loop in the relative pressure range between 0.4 and 1.0, implying that this material had very regular mesoporous channels. Based on the surface texture data (Table 3), HK was observed to have a mesopore area

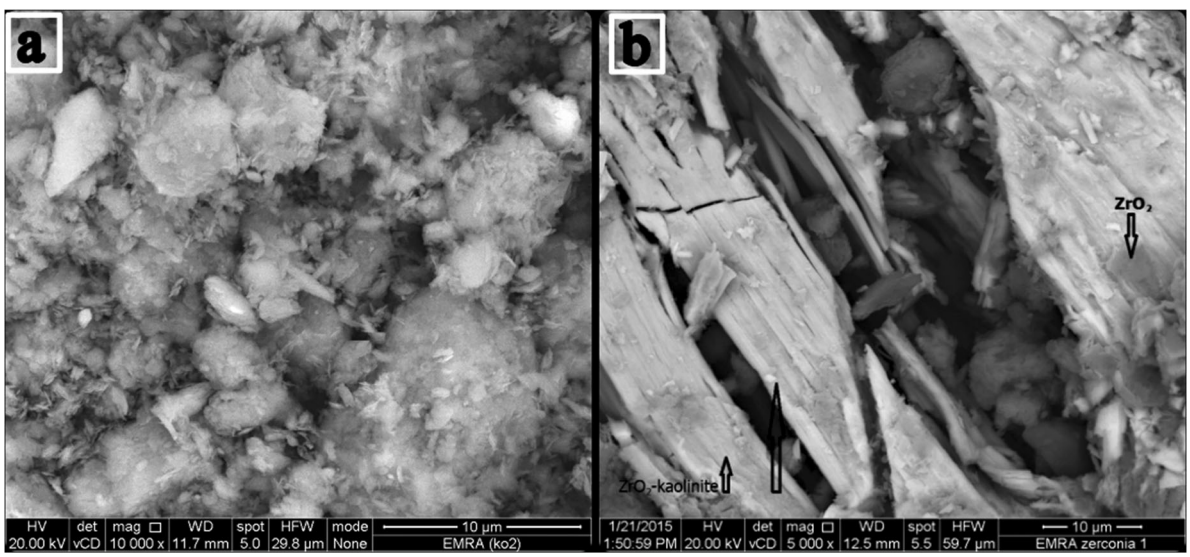

Fig. 4 SEM images of **a**HCl-treated kaolinite (HK) and **b** its Zr-intercalated sample HKZS300

https://doi.org/10.1007/s42860-021-00134-9 Published online by Cambridge University Press

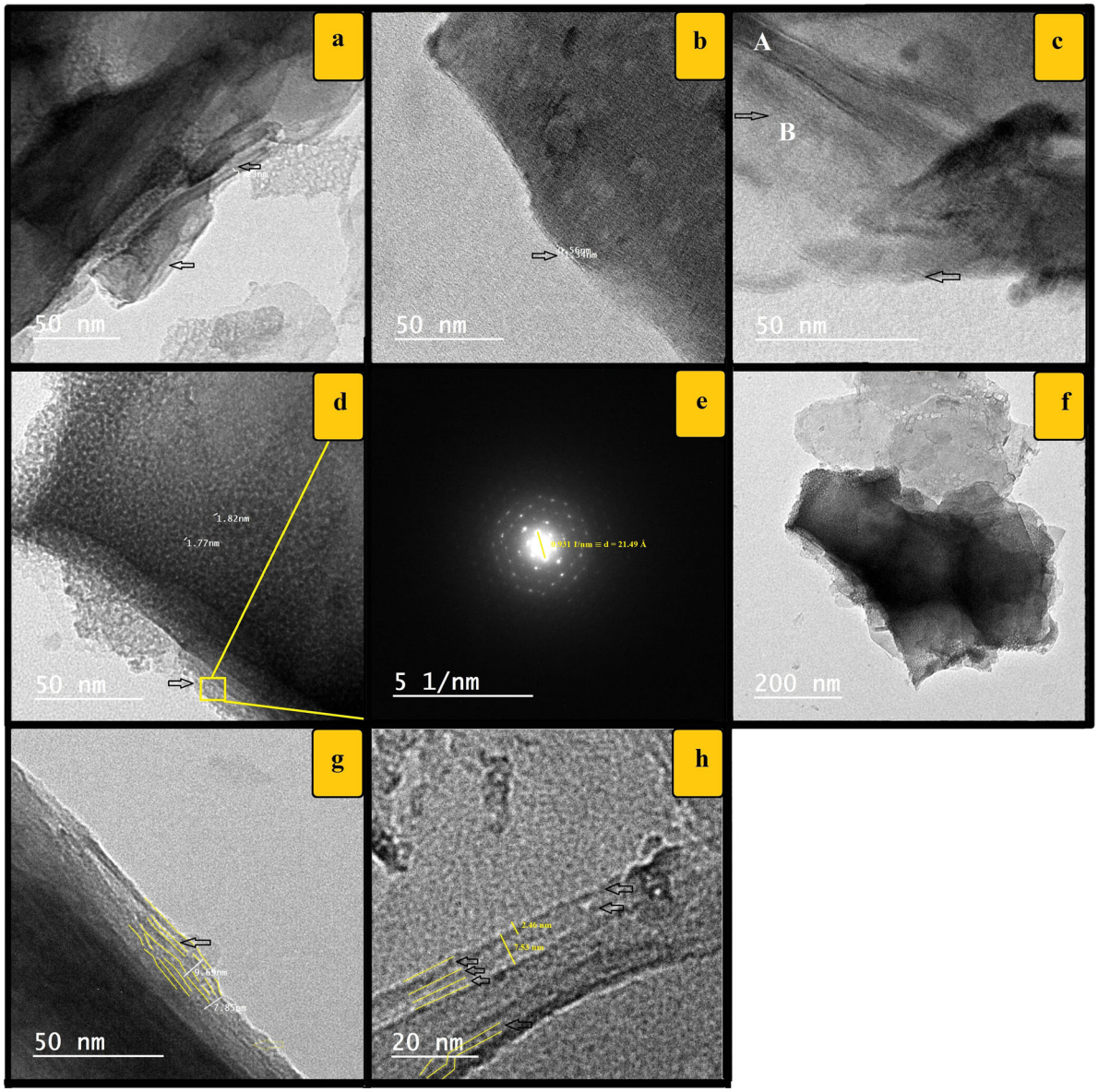

Fig. 5. TEM images **a**–**h** of Zr-intercalated sample HKZS300. TEM-SAED pattern of kaolinite layers in part **d** is shown in part **e**. The arrows indicate examples of enlarged interlayer spacings while the yellow lines show some perturbed and enlarged layers. Calculations written in yellow were made by *ImageJ* software

of 24.17 m^2 g^{-1} and mesopore volumes of 0.125 cm^3 g^{-1}, which are in good agreement with the results reported by Drweesh et al. (2016).

The adsorption isotherm of HKZS300 (Fig 7a) was estimated to be Type-II, based on the IUPAC classification of sorption isotherms, indicating the existence of mesoporosity. In addition, an obvious type H4 hysteresis loop can also be seen in the relative vapor pressure range of 0.4–1.0 bar, indicating the presence of a hierarchical micro/mesoporous system (Valášková et al., 2013). This was further ascertained by the BJH pore-size distribution plot (Fig. 5b) which confirmed the presence of micropores with an average size of ~1.83 nm and mesopores with an average size of ~3.98 nm. The HKZS300 sample showed a total surface area of 59.74 m^2 g^{-1} with micro- and mesoporous surface areas of 23.68 and 36.06 m^2 g^{-1}, respectively. The total pore volume of the sample was 0.072 cm^3 g^{-1} in which the micro- and mesoporous volumes were 0.009 cm^3 g^{-1} and 0.063 cm^3 g^{-1}, respectively. In other words, the bulk of the total surface area and pore volume of HKZS300 was derived from mesopores. Such a mesoporous structure would be favorable for adsorption purposes in terms of improved accessibility of the adsorbent to the active binding centers within the porous structure of HKZS300, as well as high diffusion rates. The increment in S_{BET} after zirconia intercalation represents an increase of ~250% over the parent surface area, which is in agreement with the morphological

https://doi.org/10.1007/s42860-021-00134-9 Published online by Cambridge University Press

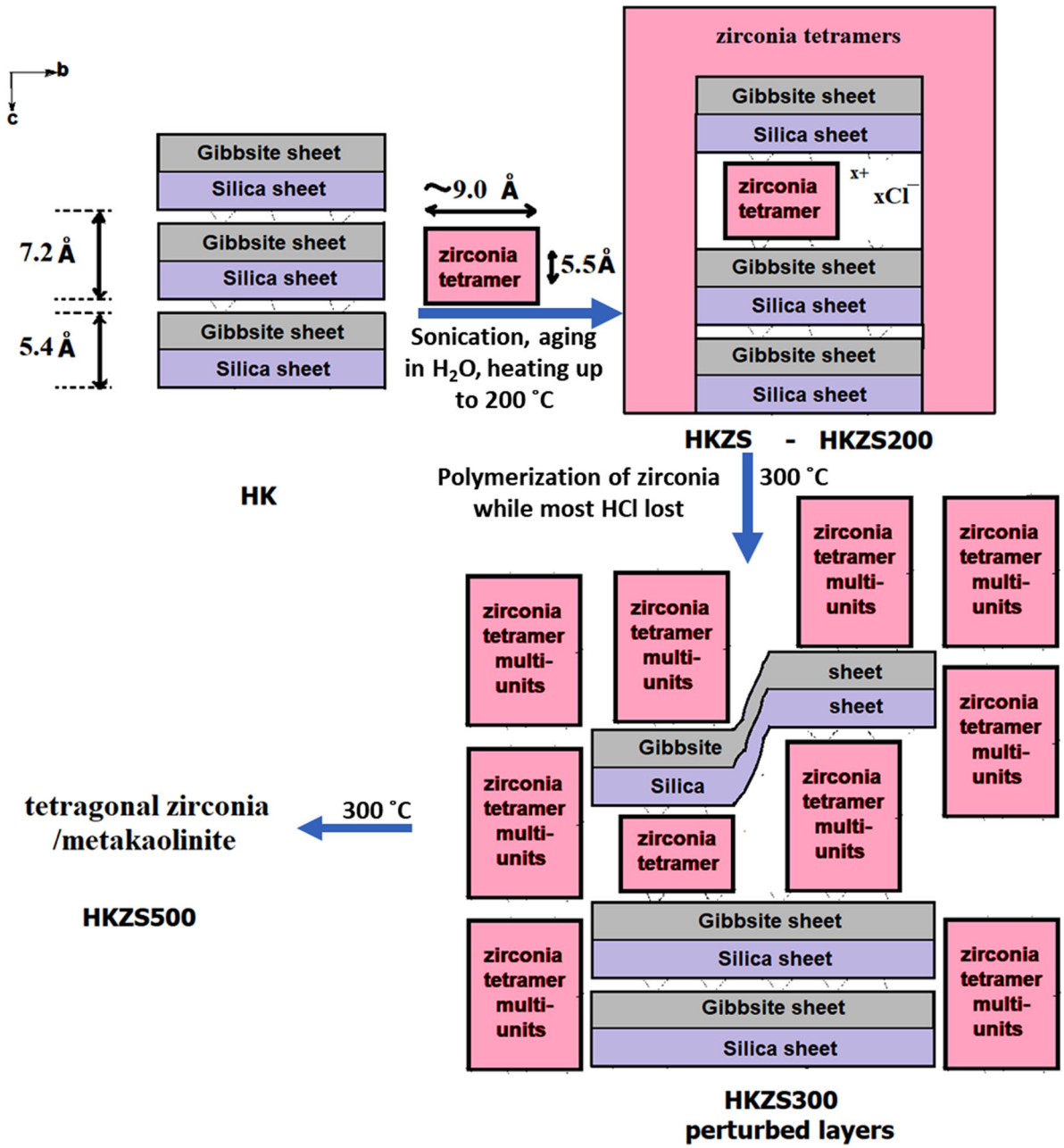

Fig. 6. Schematic representation of $ZrOCl_2 \cdot 8H_2O$ intercalation into kaolinite layers and its temperature dependence

changes observed in TEM images. According to previous studies, the acid-activated samples HK and HKZS300 were selected for comparing their properties in the adsorption study of the Cd^{2+}, Cu^{2+}, and Pb^{2+}, due to their confirmed reduced trace-metal contents, and the remarkable influence of zirconia on the kaolinite structure compared with the inactivated samples.

Cd^{2+}, Cu^{2+}, and Pb^{2+} Removal Using HK and HKZS300

A preliminary adsorption study was performed to show the improvement of the kaolin properties after intercalation with zirconia. The effect of pH on the removal of some selected heavy metals (Cd^{2+}, Cu^{2+}, and Pb^{2+}) by HK and HKZS300 (Figs 8 and 9) was investigated. The removal efficiencies were enhanced by increasing the pH of the medium, which may indicate the electrostatic nature of the adsorption process. A comparison of the removal efficiencies of HK and HKZS300 toward Cd^{2+}, Cu^{2+}, and Pb^{2+}(Fig. 8) was performed at pH 5 and 8. Small differences between the capture of Cu^{2+} and Cd^{2+} ions on HK and/or HKZS300 were observed, while Pb^{2+} showed much greater capture. The removal percentages were generally enhanced using the zirconia-modified kaolin

https://doi.org/10.1007/s42860-021-00134-9 Published online by Cambridge University Press

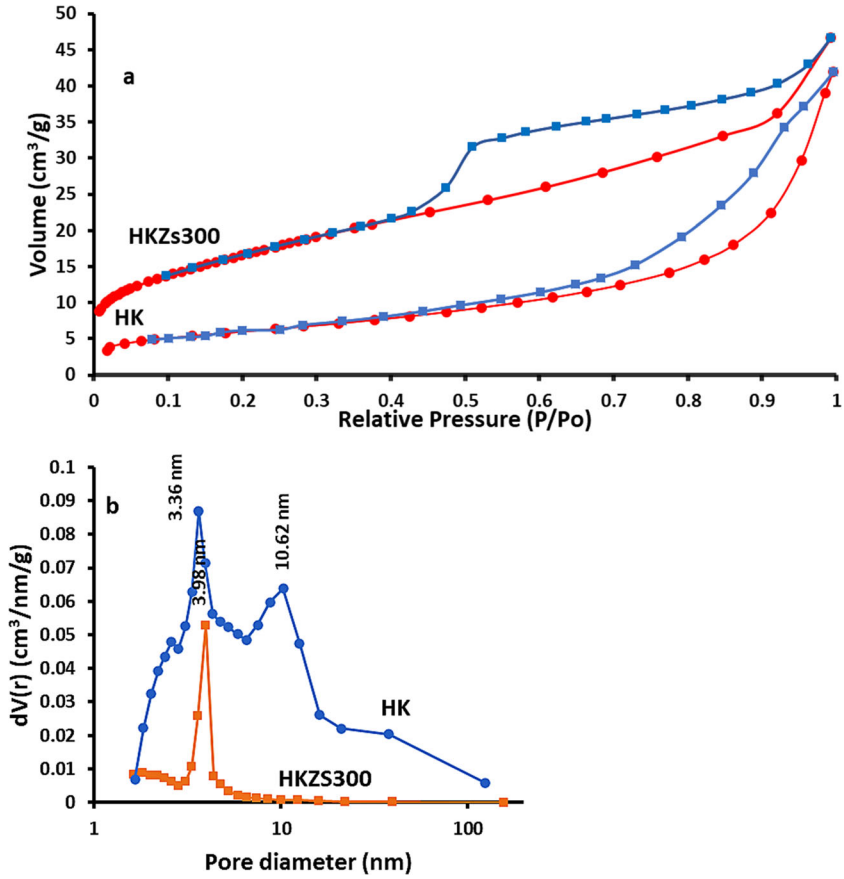

Fig. 7. **a** N_2 isothermal adsorption and desorption profiles and **b** pore-size distribution plots for HK and HKZS300 samples

HKZS300 and by increasing the initial pH of the medium. The greatest removal percentages were achieved at pH 8; on HK and HKZS300 the removal percentages for Cd^{2+} were 8.99 and 14.29%; for Cu^{2+}, 19.17 and 25.95%; and for Pb^{2+}, the values were 23.22 and 79.44%, respectively.

The estimated K_d values for the Pb^{2+}, Cu^{2+}, and Cd^{2+} adsorbed on HKZS300 at pH 8 were 3865, 350, and 169 mL g^{-1}, respectively. These distribution coefficients followed the order $Pb^{2+} >> Cu^{2+} > Cd^{2+}$, which has the same trend in terms of the removal percentages. This trend was also observed by other authors; Chen et al. (2010) investigated the ability of nano-hydroxylapatite to adsorb Pb^{2+}, Cu^{2+}, and Cd^{2+} in solution and reported similar results for zirconia-intercalated kaolinite. The K_d values seemed to be inversely proportional to the hydrated ionic radii of the metals, being Pb^{2+} (4.01 Å) > Cu^{2+} (4.19 Å) > Cd^{2+} (4.26 Å) (Berger & Hubbell, 1998). This is in agreement

Table 3. Surface texture parameters of HK and its zirconia-modified product HKZS300

Sample	HK	HKZS300
Total surface area (m^2/g)	24.17	59.74
Micropore area (m^2/g)	–	23.68
Mesopore area (m^2/g)	24.17	36.06
Total pore volume (cm^3/g)	0.125	0.072
Micropore volume (cm^3/g)	–	0.009
Mesopore volume (cm^3/g)	0.125	0.063
Micropore size (nm)	–	1.83
Mesopore size (nm)	3.63, 10.62	3.98

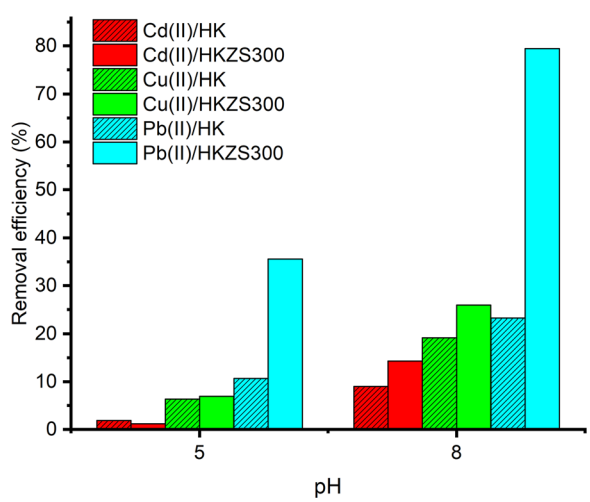

Fig. 8. Removal efficiency of Cd^{2+}, Cu^{2+}, and Pb^{2+} on HK and HKZS300 as a function of pH

https://doi.org/10.1007/s42860-021-00134-9 Published online by Cambridge University Press

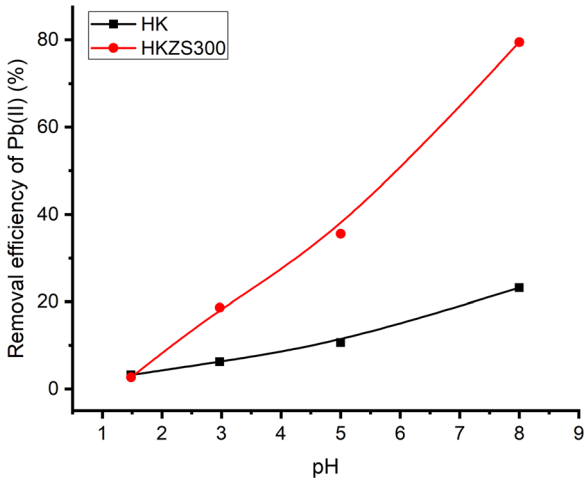

Fig. 9. Removal efficiency of Pb^{2+} on HK and HKZS300 as a function of pH

with the results reported previously by others (Lee & Moon, 2001; Chen et al., 2010) that the small ionic radius and large valence of adsorbate ions enhance their adsorption. In contrast, the smaller the ion's hydration, the closer it is to the adsorbing surface and consequently it has greater adsorption strength.

The corresponding selectivity coefficients ($S_{M1/M2}$) were 11.03, 23.16, and 2.10 at pH 8 and 7.39, 46.71, and 6.33 at pH 5 for Pb/Cu, Pb/Cd, and Cu/Cd, respectively. The results obtained showed clearly that the kaolin samples demonstrated greater efficiency for the removal of Pb^{2+} than of Cu^{2+} and Cd^{2+}. Moreover, the removal selectivity of Pb was enhanced significantly upon intercalation of kaolin with zirconia; this may be due to the larger surface area and the increased number of mesoporous active sites of HKZS300 compared with HK. The order of selectivity for metal ion removal was Pb^{2+} >> Cu^{2+} > Cd^{2+}. The comparison of the removal efficiencies of HK and HKZS300 for Pb^{2+}(Fig. 9) was performed at various pH values. Obviously, the greatest adsorption on either HK or ZrO_2-intercalated kaolinite (HKZS300) was obtained for the most basic pH, 8. When the pH varied from 1.48 to 8.0, the removal percentage of Pb^{2+} increased drastically from 3.22 to 23.22% and from 2.66 to 79.44% for HK and ZrO_2-intercalated kaolinite, respectively. These results showed that the pH of the solution greatly affected the adsorption of Pb^{2+} onto the ZrO_2-intercalated kaolin more than that of the HK.

These variations in adsorption could be explained by competition between Pb^{2+} and H_3O^+ for the surface adsorption sites (Gupta & Bhattacharyya, 2008). In general, oxygen groups on the clay surface are presumed to have the ability to bind electrolyte cations (ions in solution) yielding surface complexes. Such surface reactions could be ascribed to the affinity of charged surface sites for ions of opposing charge via the coulombic interaction between them (Miehé-Brendlé et al., 1997; Kenne Dedzo & Detellier, 2017). At low pH, the number of H_3O^+ ions exceeds that of Pb^{2+} and the surface is almost covered with H_3O^+ ions, leading to a decline in the number of Pb^{2+} ions adsorbed. Upon an increase in pH, H_3O^+ ions leave the clay surface, exposing surface sites that then become accessible to Pb^{2+}, thus enhancing ion-binding to the clay surface through a mechanism like that of ion-exchange (H_3O^+/Pb^{2+}). The significant improvement in terms of the percentages of metal ions removed using the acid-activated kaolinite intercalated with zirconia (HKZS300) vs. the unchanged, acid-activated kaolinite (HK) is mainly related to intercalation of zirconia into kaolinite via adsorption up to pH 5, while a precipitation process may be invoked at greater pH (8). This modification provides new, accessible active sites and alters significantly the textural properties which enhance the limited sorptivity of kaolinite. Such heavy-metal uptake enhancement with rising pH has also been reported for natural kaolin and orthophosphate-modified kaolin (Jiang et al., 2010), which could be assigned to the deprotonation of edge-OH groups on the adsorbent surfaces with increasing pH, as demonstrated in a recent pH-metric titration study (Drweesh et al., 2016). Accordingly, at low pH, an electrostatic repulsion arises between the metal cations and the protonated kaolinite edge-OH groups (e.g. $SiOH_2^+$ exists at low pH). On the other hand, the conditions are reversed to electrostatic attraction of the metal cations to the deprotonated surface Al–OH, Si–OH, and Zr–OH groups at high pH. A precipitation process of the metal hydroxides could also accompany the adsorption at high pH.

CONCLUSIONS

The intercalation of zirconia into the interlayer space of Egyptian kaolinite was suggested as a good method of synthesizing zirconia-loaded kaolin with a preference for acid-activated kaolin. The new material had an enlarged basal spacing of ~11–25 Å in HKZS300, which is suggested to be due to the intercalated zirconia oligomers bonded with kaolinite layers through aluminol groups up to 300°C, giving rise to a significantly perturbed zirconia/kaolinite layered structure. At 500°C, zirconia crystallized in a tetragonal phase while kaolinite decomposed to metakaolinite. The intercalation process caused a remarkable increase in the surface area of the kaolin, an improvement of the layer stacking, and a uniform distribution of Zr among all of the kaolinite particles. In addition, the intercalation process created new micropores which led to the observed increase in surface area but decreased pore volume and pore-size distribution due to the new micropore creation. The metal sorption characteristics of the ZrO_2-modified kaolin was confirmed to be much more efficient than the raw or activated kaolin for the removal of Pb^{2+}, Cu^{2+}, and Cd^{2+} with a 300% improvement in the removal efficiency and a greater selectivity for removal of Pb with the order: Pb^{2+} >> Cu^{2+} > Cd^{2+}.

The catalytic activity of zirconia-intercalated kaolinite offers much interest for further research.

https://doi.org/10.1007/s42860-021-00134-9 Published online by Cambridge University Press

SUPPLEMENTARY INFORMATION

The online version contains supplementary material available at https://doi.org/10.1007/s42860-021-00134-9.

ACKNOWLEDGMENTS

The authors are grateful to the Editor in Chief and the anonymous reviewers for their constructive criticism and valuable comments which helped to improve the manuscript. The authors are also grateful to the National Research Centre, Egypt, for partial financial support of this study via project No AR110903.

FUNDING

Funding sources are as stated in the Acknowledgments.

Declarations

Conflict of Interest

The authors declare that they have no conflict of interest.

REFERENCES

Abou-El-Sherbini, K. S., Elzahany, E. A. M., Wahba, M. A., Drweesh, S. A., & Youssef, N. S. (2017). Evaluation of some intercalation methods of dimethylsulphoxide onto HCl-treated and untreated Egyptian kaolinite. *Applied Clay Science, 137*, 33–42.

Agarkov, D., Burmistrov, I., Tsybrov, F., Tartakovskii, I., Kharton, V., & Bredikhin, S. (2018). In-situ Raman spectroscopy analysis of the interface between ceria-containing SOFC anode and stabilized zirconia electrolyte. *Solid State Ionics, 319*, 125–129.

Bailey, S. W. (1966). The status of clay mineral structures. Pp. 1–23 in *Clays and Clay Minerals Proceedings of the Fourteenth National Conference, Berkeley, California* (S. W. Bailey, editor). Pergamon.

Baird, R. B., Eaton, A. D., & Rice, E. W. (2017). Standard Methods for the Examination of Water and Wastewater. (23rd edition). American Water Works Association; Water Pollution Control Federation; Water Environment Federation, Washington.

Barrett, E. P., Joyner, L. G., & Halenda, P. P. (1951). The determination of pore volume and area distributions in porous substances. I. Computations from nitrogen isotherms. *Journal of the American Chemical Society, 73*, 373–380.

Beden, B., & Guillaum, I. (1969). Thermal decomposition of zirconyl chloride octahydrate in ambient air. *Comptes rendus hebdomadaires des seances de l academie des sciences series c, 269*, 1629–1669.

Berger, M., & Hubbell, J. (1998). *1999 Photon Attenuation Coefficients* CRC Handbook of Chemistry and Physics 79th edn, (D R. Lide, editor). CRC Press, Boca Raton, Florida, USA.

Bhattacharyya, K. G., & Gupta, S. S. (2006). Kaolinite, montmorillonite, and their modified derivatives as adsorbents for removal of Cu (II) from aqueous solution. *Separation and Purification Technology, 50*, 388–397.

Bhattacharyya, K. G., & Gupta, S. S. (2008). Adsorption of Fe(III), Co(II) and Ni(II) on ZrO-kaolinite and ZrO-montmorillonite surfaces in aqueous medium. *Colloids and Surfaces A: Physicochemical and Engineering Aspects, 317*, 71–79.

Brunauer, S., Emmett, P. H., & Teller, E. (1938). Adsorption of gases in multimolecular layers. *Journal of the American Chemical Society, 60*, 309–319.

Chaabene, S. B., Bergaoui, L., & Ghorbel, A. (2004). Zirconium and sulfated zirconium pillared clays: a combined intercalation solution study and solid characterization. *Colloids and Surfaces A: Physicochemical and Engineering Aspects, 251*, 109–115.

Chen, S. B., Ma, Y. B., Chen, L., & Xian, K. (2010). Adsorption of aqueous Cd(II), Pb(II), Cu(II) ions by nano-hydroxyapatite: single- and multi-metal competitive adsorption study. *Geochemical Journal, 44*, 233–239.

Cheng, H., Liu, Q., Cui, X., Zhang, Q., Zhang, Z., & Frost, R. L. (2012). Mechanism of dehydroxylation temperature decrease and high temperature phase transition of coal-bearing strata kaolinite intercalated by potassium acetate. *Journal of Colloid and Interface Science, 376*, 47–56.

Chevalier, J., Gremillard, L., Virkar, A. V., & Clarke, D. R. (2009). The tetragonal-monoclinic transformation in zirconia: lessons learned and future trends. *Journal of the American Ceramic Society, 92*, 1901–1920.

Dedzo, G. K., & Detellier, C. (2016). Functional nanohybrid materials derived from kaolinite. *Applied Clay Science, 130*, 33–39.

Drweesh, S. A., Fathy, N. A., Wahba, M. A., Hanna, A. A., Akarish, A. I. M., Elzahany, E. A. M., El-Sherif, I. Y., & Abou-El-Sherbini, K. S. (2016). Equilibrium, kinetic and thermodynamic studies of Pb(II) adsorption from aqueous solutions on HCl-treated Egyptian kaolin. *Journal of Environmental Chemical Engineering, 4*, 1674–1684.

Farfan-Torres, E., Sham, E., & Grange, P. (1992). Pillared clays: preparation and characterization of zirconium pillared montmorillonite. *Catalysis Today,15,* 515–526.

Farmer, V. C., & Russell, J. D. (1964). The infra-red spectra of layer silicates. *Spectrochimica Acta, 20*, 1149–1173.

Frost, R. L., & Vassallo, A. M. (1996). The dehydroxylation of the kaolinite clay minerals using infrared emission spectroscopy. *Clays and Clay Minerals, 44*, 635–651.

Frost, R. L., Kristof, J., Paroz, G. N., Tran, T. H., & Kloprogge, J. T. (1998). The role of water in the intercalation of kaolinite with potassium acetate. *Journal of Colloid and Interface Science, 204*, 227–236.

Gao, W., Zhao, S., Wu, H., Deligeer, W., & Asuha, S. (2016). Direct acid activation of kaolinite and its effects on the adsorption of methylene blue. *Applied Clay Science, 126*, 98–106.

Gil, A., Vicente, M., Lambert, J.-F., & Gandıa, L. (2001). Platinum catalysts supported on Al-pillared clays: Application to the catalytic combustion of acetone and methyl-ethyl-ketone. *Catalysis today, 68*, 41–51.

Gong, L., Sun, L.-B., Sun, Y.-H., Li, T.-T., & Liu, X.-Q. (2011). Exploring in situ functionalization strategy in a hard template process: Preparation of sodium-modified mesoporous tetragonal zirconia with superbasicity. *The Journal of Physical Chemistry C, 115*, 11633–11640.

Gorodylova, N., & Šulcová, P. (2018). DTA-TGA and XRD study of the formation of LISICON-type $Li_{1+x}Cr_xZr_{2-x}(PO_4)_3$ ceramic using $ZrOCl_2{\cdot}8H_2O$ as precursor. *Journal of Thermal Analysis and Calorimetry, 133*, 405–411.

Gorodylova, N., Šulcová, P., Bosacka, M., & Filipek, E. (2014). DTA-TG and XRD study on the reaction between $ZrOCl_2{\cdot}8H_2O$ and $(NH_4)_2HPO_4$ for synthesis of ZrP_2O_7. *Journal of Thermal Analysis and Calorimetry, 118*, 1095–1100.

Grzybek, T., Klinik, J., Olszewska, D., Papp, H., & Smarzowski, J. (2001). The influence of montmorillonite treatment on structure, sorption properties and catalytic behaviour: Part I. Zirconia pillared clays modified with manganese as Denox catalysts. *Polish Journal of Chemistry, 75*, 857–868.

Gupta, S. S., & Bhattacharyya, K. G. (2005). Interaction of metal ions with clays: I. A case study with Pb(II). *Applied Clay Science, 30*, 199–208.

Gupta, S. S., & Bhattacharyya, K. G. (2006). Removal of Cd(II) from aqueous solution by kaolinite, montmorillonite and their poly (oxo zirconium) and tetrabutylammonium derivatives. *Journal of Hazardous Materials, 128*, 247–257.

Gupta, S. S., & Bhattacharyya, K. G. (2008). Immobilization of Pb (II), Cd (II) and Ni (II) ions on kaolinite and montmorillonite surfaces from aqueous medium. *Journal of Environmental Management, 87*, 46–58.

Ianchis, R., Corobea, M., Donescu, D., Rosca, I., Cinteza, L., Nistor, L., Vasile, E., Marin, A., & Preda, S. (2012). Advanced functionalization of organoclay nanoparticles by silylation and their polystyrene nanocomposites obtained by miniemulsion polymerization. *Journal of Nanoparticle Research, 14*, 1–12.

Ilić, B. R., Mitrović, A. A., & Miličić, L. R. (2010). Thermal treatment of kaolin clay to obtain metakaolin. *Hemijska industrija, 64*, 351–356.

Jiang, M.-q., Jin, X.-y., Lu, X.-q., & Chen, Z.-l. (2010). Adsorption of Pb(II), Cd(II), Ni(II) and Cu(II) onto natural kaolinite clay. *Desalination, 252*, 33–39.

Jiang, H., Liu, G., Hu, Y., Xu, L., Yu, Y., Xie, Z., & Chen, H. (2013). Flotation and adsorption of quaternary ammonium salts collectors on kaolinite of different particle size. *International Journal of Mining Science and Technology, 23*, 249–253.

Kenne Dedzo, G., & Detellier, C. (2017). Characterization and Applications of Kaolinite Robustly Grafted by an Ionic Liquid with Naphthyl Functionality. *Materials (Basel, Switzerland), 10*, 1006.

Kristó, J., Frost, R. L., Felinger, A., & Mink, J. (1997). FTIR spectroscopic study of intercalated kaolinite. *Journal of Molecular Structure, 410*, 119–122.

Kristóf, T., Sarkadi, Z., Ható, Z., & Rutkai, G. (2018). Simulation study of intercalation complexes of kaolinite with simple amides as primary intercalation reagents. *Computational Materials Science, 143*, 118–125.

Ledoux, R. L., & White, J. L. (1966). Infrared studies of hydrogen bonding interaction between kaolinite surfaces and intercalated potassium acetate, hydrazine, formamide, and urea. *Journal of Colloid and Interface Science, 21*, 127–152.

Lee, D. H., & Moon, H. (2001). Adsorption equilibrium of heavy metals on natural zeolites. *Korean Journal of Chemical Engineering, 18*, 247–256.

Libowitzky, E. (1999). Correlation of O-H stretching frequencies and O-H O hydrogen bond lengths in minerals. Pp. 103–115 in: *Hydrogen Bond Research* (P. Schuster & W. Mikenda, editors). Springer, Vienna.

Libowitzky, E., & Beran, A. (2004). IR spectroscopic characterisation of hydrous species in minerals. *Spectroscopic Methods in Mineralogy, 6*, 227–279.

Majd, M. T., Davoudi, M., Ramezanzadeh, M., Ghasemi, E., Ramezanzadeh, B., & Mahdavian, M. (2020). Construction of a smart active/barrieranti-corrosion system based on epoxy-ester/zinc intercalated kaolin nanocontainer for steel substrate. *Construction and Building Materials, 247*, 118555.

Makó, É., Kovács, A., Katona, R., & Kristóf, T. (2016). Characterization of kaolinite-cetyltrimethylammonium chloride intercalation complex synthesized through eco-friend kaolinite-urea pre-intercalation complex. *Colloids and Surfaces A: Physicochemical and Engineering Aspects, 508*, 265–273.

Matsui, K., & Ohgai, M. (2002). Formation Mechanism of Hydrous Zirconia Particles Produced by Hydrolysis of $ZrOCl_2$ Solutions: IV, Effects of $ZrOCl_2$ Concentration and Reaction Temperature. *Journal of the American Ceramic Society, 85*, 545–553.

Miehé-Brendlé, J., Khouchaf, L., Baron, J., Le Dred, R., & Tuilier, M. H. (1997). Zr-exchanged and pillared beidellite: preparation and characterization by chemical analysis, XRD and Zr K EXAFS. *Microporous Materials, 11*, 171–183.

Miura, N., Sato, T., Anggraini, S. A., Ikeda, H., & Zhuiykov, S. (2014). A review of mixed-potential type zirconia-based gas sensors. *Ionics, 20*, 901–925.

Mnasri, S., & Frini-Srasra, N. (2013). Synthesis, characterization and catalytic evaluation of zirconia-pillared bentonite for 1, 3-dioxalane synthesis. *Surface Engineering and Applied Electrochemistry, 49*, 336–347.

Nagarajan, V., & Rao, K. (1990). Thermally induced chemical and structural changes in alumina-zirconia-silica gels during the formation of ceramic composites. *Journal of Solid State Chemistry, 88*, 419–428.

Ngnie, G., Dedzo, G. K., & Detellier, C. (2016). Synthesis and catalytic application of palladium nanoparticles supported on kaolinite-based nanohybrid materials. *Dalton transactions, 45*, 9065–9072.

Ohtsuka, K., Hayashi, Y., & Suda, M. (1993). Microporous zirconia-pillared clays derived from three kinds of zirconium polynuclear ionic species. *Chemistry of Materials, 5*, 1823–1829.

Olejnik, S., Aylmore, L. A. G., Posner, A. M., & Quirk, J. P. (1968). Infrared spectra of kaolin mineral-dimethyl sulfoxide complexes. *The Journal of Physical Chemistry, 72*, 241–249.

Sari, A., & Tuzen, M. (2014). Cd(II) adsorption from aqueous solution by raw and modified kaolinite. *Applied Clay Science, 88–89*, 63–72.

Shirsath, S. R., Patil, A. P., Patil, R., Naik, J. B., Gogate, P. R., & Sonawane, S. H. (2013). Removal of Brilliant Green from wastewater using conventional and ultrasonically prepared poly(acrylic acid) hydrogel loaded with kaolin clay: A comparative study. *Ultrasonics Sonochemistry, 20*, 914–923.

Singh, B. & Mackinnon, I. D. (1999). Intercalation of kaolins by alkaline earth metal salts. Pp. 489–495 in *11th International Clay Conference, Ottawa.*

Solovkin, A. S., & Tsvetkova, Z. N. (1962). The chemistry of aqueous solutions of zirconium salts (Does the zirconyl ion exist?). *Russian Chemical Reviews, 31*, 655–699.

Štefanić, G., Musić, S., Popović, S., & Furić, K. (1996). Formation of ZrO_2 by the thermal decomposition of zirconium salts. *Croatica Chemica Acta,69,* 223–239.

Swindale, L. D. (1975). The crystallography of minerals of the kaolin group. Pp. 121–154 in *Soil Components: Vol. 2: Inorganic Components* (J. E. Gieseking, editor). Springer, Berlin Heidelberg.

Takagi, S. (1954). Zirconium compounds. I. Thermal decomposition of zirconium chloride octahydrate. *Journal of the Chemical Society of Japan, 75*, 637–639.

Tunney, J. J., & Detellier, C. (1993). Interlamellar covalent grafting of organic units on kaolinite. *Chemistry of Materials, 5*, 747–748.

Valášková, M., Tokarský, J., Hundáková, M., Zdrálková, J., & Smetana, B. (2013). Role of vermiculite and zirconium–vermiculite on the formation of zircon–cordierite nanocomposites. *Applied Clay Science, 75*, 100–108.

Valverde, J. L., de Lucas, A., Sánchez, P., Dorado, F., & Romero, A. (2003). Cation exchanged and impregnated Ti-pillared clays for selective catalytic reduction of NOx by propylene. *Applied Catalysis B: Environmental, 43*, 43–56.

Vaughan, D. E. (1994). *Pillared interlayered kandite clay compositions*. Google Patents.

Vera, C. R., Pieck, C. L., Shimizu, K., & Parera, J. M. (2002). Tetragonal structure, anionic vacancies and catalytic activity of SO_4^{2-}-ZrO_2 catalysts for n-butane isomerization. *Applied Catalysis A: General, 230*, 137–151.

Wada, K. (1961). Lattice expansion of kaolin minerals by treatment with potassium acetate. *American Mineralogist: Journal of Earth and Planetary Materials, 46*, 78–91.

Wang, X., Liu, T., Yu, J., Li, L., & Zhang, X. (2019). A new application of $Ce_xZr_{1-x}O_2$ as dense diffusion barrier in limiting current oxygen sensor. *Sensors and Actuators B: Chemical, 285*, 391–397.

Zaharia, A., Perrin, F.-X., Teodorescu, M., Radu, A.-L., Iordache, T.-V., Florea, A.-M., Donescu, D., & Sarbu, A. (2015). New organophilic kaolin clays based on single-point grafted 3-aminopropyl dimethylethoxysilane. *Physical Chemistry Chemical Physics, 17*, 24908–24916.

Zhang, Q.-h., Chen, G.-q., & Xing, T.-l. (2017). Silk flame retardant finish by ternary silica sol containing boron and nitrogen. *Applied Surface Science, 421*, 52–60.

(Received 6 May 2020; revised 5 May 2021; AE: Prakash B. Malla)